J. Fluid Mech. (2023), *vol*. 958, A26, doi:10.1017/jfm.2023.55

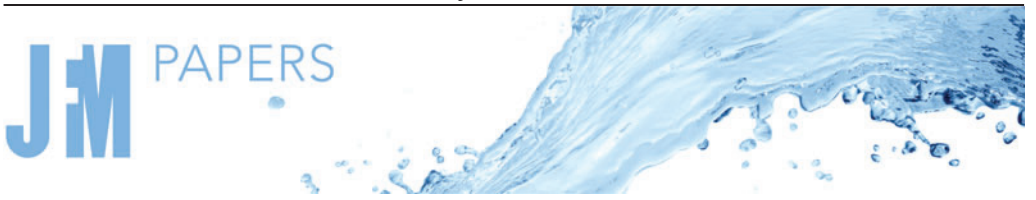

When does an impacting drop stop bouncing?

Vatsal Sanjay[1],†, **Pierre Chantelot**[1],† **and Detlef Lohse**[1,2],†

[1]Physics of Fluids Group, Max Planck Center for Complex Fluid Dynamics, Department of Science and Technology, and J. M. Burgers Centre for Fluid Dynamics, University of Twente, P. O. Box 217, 7500 AE Enschede, The Netherlands

[2]Max Planck Institute for Dynamics and Self-Organization, Am Fassberg 17, 37077 Göttingen, Germany

(Received 11 August 2022; revised 21 November 2022; accepted 15 December 2022)

Non-wetting substrates allow impacting liquid drops to spread, recoil and take-off, provided they are not too heavy (Biance *et al.*, *J. Fluid Mech.*, vol. 554, 2006, pp. 47–66) or too viscous (Jha *et al.*, *Soft Matt.*, vol. 16, no. 31, 2020, pp. 7270–7273). In this article, using direct numerical simulations with the volume of fluid method, we investigate how viscous stresses and gravity oppose capillarity to inhibit drop rebound. Close to the bouncing to non-bouncing transition, we evidence that the initial spreading stage can be decoupled from the later retraction and take-off, allowing us to understand the rebound as a process converting the surface energy of the spread liquid into kinetic energy. Drawing an analogy with coalescence-induced jumping, we propose a criterion for the transition from the bouncing to the non-bouncing regime, namely by the condition $Oh_c + Bo_c \sim 1$, where Oh_c and Bo_c are the Ohnesorge number and Bond number at the transition, respectively. This criterion is in excellent agreement with the numerical results. We also elucidate the mechanisms of bouncing inhibition in the heavy and viscous drop limiting regimes by calculating the energy budgets and relating them to the drop's shape and internal flow.

Key words: drops

1. Introduction

Evidence of scientists' fascination for drop impacts can be traced back to the sketch of a water drop splashing onto a sheet of paper by Leonardo da Vinci in the margin of folio 33r in Codex Hammer/Leicester (1506–1510) (da Vinci 1508). In particular, the striking patterns created by drop fragmentation, at high impact velocity, have attracted attention (Rein 1993; Xu, Zhang & Nagel 2005; Yarin 2006; Villermaux & Bossa 2011; Josserand

† Email addresses for correspondence: vatsalsanjay@gmail.com, p.r.a.chantelot@utwente.nl, d.lohse@utwente.nl

& Thoroddsen 2016; Kim *et al.* 2020). Lower velocity impacts, although they do not cause drops to shatter, also give rise to a rich variety of phenomena (Worthington 1877*a*,*b*; Chandra & Avedisian 1991; Yarin 2006; Thoroddsen, Etoh & Takehara 2008; Josserand & Thoroddsen 2016). The rebound of drops on non-wetting substrates may be one of the most fascinating of such interactions (Richard & Quéré 2000; Richard, Clanet & Quéré 2002; Tsai *et al.* 2009; Nair *et al.* 2014).

Upon impact, the liquid first spreads (Philippi, Lagrée & Antkowiak 2016; Gordillo, Sun & Cheng 2018) until it reaches its maximal extent (Clanet *et al.* 2004; Laan *et al.* 2014; Wildeman *et al.* 2016; Gordillo, Riboux & Quintero 2019). It then recoils, following a Taylor–Culick-type retraction parallel to the substrate (Taylor 1959; Culick 1960; Bartolo, Josserand & Bonn 2005; Deka & Pierson 2020; Pierson *et al.* 2020; Sanjay *et al.* 2022), and ultimately bounces off in an elongated shape perpendicular to the substrate (Richard & Quéré 2000; Yarin 2006; Josserand & Thoroddsen 2016).

Such rebounds abound in nature, as non-wetting surfaces provide plants and animals a natural way to keep dry (Neinhuis & Barthlott 1997; Quéré 2008), and are relevant in many industrial processes such as inkjet printing (Lohse 2022). In some applications, it is pertinent that drops ricochet off the surface, such as in self-cleaning (Blossey 2003), keeping clothes dry (Liu, Chen & Xin 2008) and anti-fogging surfaces (Mouterde *et al.* 2017*a*). However, in most cases, bouncing must be suppressed. For example, in cooling applications (Kim 2007; Shiri & Bird 2017; Jowkar & Morad 2019) and pesticide spraying in agriculture (Bergeron *et al.* 2000; He *et al.* 2021; Gorin *et al.* 2022). It is therefore natural to wonder when a drop stops bouncing.

Thus, when does the bouncing stop? On the one hand, Biance *et al.* (2006) found that heavy drops, i.e. drops larger than their gravito-capillary length $l_c = \sqrt{\gamma/\rho_d g}$, where γ is the drop–air surface tension coefficient, ρ_d is the density of the drop and g is the acceleration due to gravity, cannot bounce. On the other hand, Jha *et al.* (2020) showed that there exists a critical viscosity, two orders of magnitude higher than that of water, beyond which aqueous drops do not bounce either, irrespective of their impact velocity. Therefore, gravity and viscosity counteract the bouncing.

In this paper, we investigate and quantify how exactly gravity and viscous stresses compete against capillarity to prevent drops from bouncing off non-wetting substrates, using direct numerical simulations. We focus on evidencing the mechanisms of bouncing inhibition, and exhibit a simple criterion delineating the bouncing to non-bouncing transition through an analogy with coalescence-induced drop jumping (Boreyko & Chen 2009; Liu *et al.* 2014; Farokhirad, Morris & Lee 2015; Mouterde *et al.* 2017*b*; Lecointre *et al.* 2019).

The paper is organised as follows: § 2 discusses the governing equations employed in this work. Section 3 explores the bouncing to non-bouncing transition and formulates a criterion for the inhibition of bouncing based on first principles, followed by § 4, which delves into the limiting cases of this criterion. The paper ends with conclusions and an outlook on future work in § 5.

2. Governing equations

We employ direct numerical simulations to study the drop impact process in an axisymmetric setting (figure 1), using the free software program *Basilisk C* (Popinet 2013–2022*a*) that employs the geometric volume of fluid (VoF) method for interface reconstruction (Popinet 2009). For an incompressible flow, the mass conservation requires the velocity field to be divergence free (tildes denote dimensionless quantities throughout

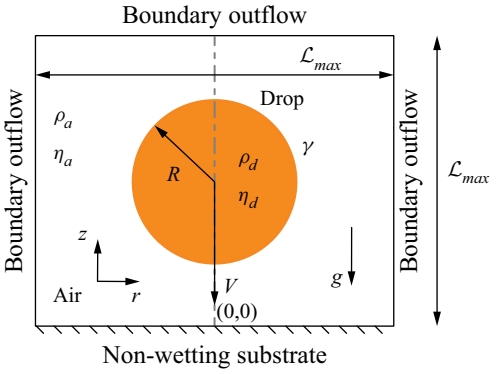

Figure 1. Axisymmetric computational domain used to study the impact of a drop with radius R and velocity V on an ideal non-wetting substrate. The subscripts d and a denote the drop and air, respectively, to distinguish their material properties, the density ρ and viscosity η. The drop–air surface tension coefficient is γ and g denotes the acceleration due to gravity. The grey dashed-dotted line represents the axis of symmetry, $r = 0$. Boundary outflow is applied at the top and side boundaries (tangential stresses, normal velocity gradient and ambient pressure are set to zero). The domain boundaries are far enough not to influence the drop impact process ($\mathcal{L}_{max} \gg R$, $\mathcal{L}_{max} = 8R$ in the worst case).

this manuscript):

$$\tilde{\boldsymbol{\nabla}} \cdot \tilde{\boldsymbol{v}} = 0, \tag{2.1}$$

where we non-dimensionalise the velocity field with the inertio-capillary velocity $V_\gamma = \sqrt{\gamma/(\rho_d R)}$. We further non-dimensionalise all lengths with the drop radius R (figure 1), time with the inertio-capillary time scale, $\tau = \sqrt{\rho_d R^3/\gamma} = R/V_\gamma$, and pressure with the capillary pressure, $p_\gamma = \gamma/R$, to write the momentum equation as

$$\frac{\partial \tilde{\boldsymbol{v}}}{\partial \tilde{t}} + \boldsymbol{\nabla} \cdot (\tilde{\boldsymbol{v}}\tilde{\boldsymbol{v}}) = \frac{1}{\tilde{\rho}}(-\tilde{\boldsymbol{\nabla}}\tilde{p}' + \tilde{\boldsymbol{\nabla}} \cdot (2Oh\tilde{\boldsymbol{\mathcal{D}}}) + \tilde{\boldsymbol{f}}), \tag{2.2}$$

where the deformation tensor $\boldsymbol{\mathcal{D}}$ is the symmetric part of the velocity gradient tensor ($= (\boldsymbol{\nabla v} + (\boldsymbol{\nabla v})^T)/2$). The Ohnesorge number Oh (the ratio of inertio-capillary to inertio-viscous time scales) and the dimensionless density $\tilde{\rho}$ are written using the one-fluid approximation (Prosperetti & Tryggvason 2009; Tryggvason, Scardovelli & Zaleski 2011) as

$$Oh = \Psi Oh_d + (1 - \Psi)Oh_a, \tag{2.3}$$

$$\tilde{\rho} = \Psi + (1 - \Psi)\frac{\rho_a}{\rho_d}, \tag{2.4}$$

where Ψ is the VoF tracer ($= 1$ for the drop and 0 otherwise), and ρ_a/ρ_d is the air–drop density ratio. Here,

$$Oh_d = \frac{\eta_d}{\sqrt{\rho_d \gamma R}} \quad \text{and} \quad Oh_a = \frac{\eta_a}{\sqrt{\rho_d \gamma R}} \tag{2.5a,b}$$

are the Ohnesorge numbers based on the viscosities of the drop liquid and of air, respectively. To minimise the influence of the surrounding medium, we keep ρ_a/ρ_d and Oh_a fixed at 10^{-3} and 10^{-5}, respectively. For a lean notation, we will use Oh instead of Oh_d in the remainder of the text.

Lastly, $\tilde{p}'$ denotes the reduced pressure field, $\tilde{p}' = \tilde{p} + Bo\tilde{\rho}\tilde{z}$, where $\tilde{p}$ and $Bo\tilde{\rho}\tilde{z}$ represent the mechanical and the hydrostatic pressures, respectively. Here, $\tilde{z}$ is the distance

away from the non-wetting substrate (see figure 1) and the Bond number Bo compares gravity with the surface tension force

$$Bo = \frac{\rho_d g R^2}{\gamma}. \tag{2.6}$$

Using this reduced pressure approach ensures an exact hydrostatic balance as described in Popinet (2018) and Popinet *et al.* (2013–2022*b*). This formulation requires an additional singular body force at the interface such that $\tilde{\boldsymbol{f}}$ takes the form (Brackbill, Kothe & Zemach 1992)

$$\tilde{\boldsymbol{f}} \approx \left(\tilde{\kappa} + Bo\left(1 - \frac{\rho_a}{\rho_d}\right)\tilde{z}\right)\tilde{\boldsymbol{\nabla}}\Psi, \tag{2.7}$$

where the first and second terms on the right-hand side are the local capillary and hydrostatic pressure jumps across the interface, respectively, with $\tilde{\kappa}$ the interfacial curvature calculated using the height-function approach (Popinet 2009).

Figure 1 shows the axisymmetric computational domain where we solve the equations discussed above. A no-slip and no-penetration boundary condition is applied on the substrate along with a zero normal pressure gradient. Here, we also impose $\Psi = 0$ to maintain a thin air layer between the drop and the substrate to model an ideal non-wetting substrate (for a detailed discussion about this method, readers are referred to Sanjay 2022*b*). Physically, this implies that the minimum thickness of this air layer is $\Delta/2$, where Δ is the minimum grid size, throughout the simulation duration. We use *Basilisk C*'s (Popinet 2013–2022*a*) adaptive mesh refinement capabilities to finely resolve regions of high velocity gradients and at the drop–air interface. We undertook a mesh independence study to ensure that the results are independent of this mesh resolution and use a minimum grid size $\Delta = R/1024$ for this study. Initially, we assume that the drop is spherical and that it impacts with a dimensionless velocity, $\tilde{V} = V/V_\gamma = \sqrt{We}$, where the impact Weber number

$$We = \frac{\rho_d R V^2}{\gamma}, \tag{2.8}$$

is the ratio of the inertial pressure during impact to the capillary pressure. We refer the readers to Popinet (2009, 2015, 2013–2022*a*), Zhang *et al.* (2022) and Sanjay (2022*a*,*b*) for details of the computational method employed in this work.

3. Bouncing inhibition

We investigate the behaviour of drops impacting on non-wetting substrates by exploring the influence of the following dimensionless parameters: the Weber number $We = \rho R V^2/\gamma$, the Bond number $Bo = \rho_d g R^2/\gamma$ and the drop Ohnesorge number $Oh = \eta_d/\sqrt{\rho_d \gamma R}$. We restrict ourselves to impacts with $We \geq 1$ and do not discuss the bouncing to non-bouncing transition observed for $We \ll 1$ (gentle deposition) (Richard & Quéré 2000; Moláček & Bush 2012; Planchette, Biance & Lorenceau 2012). In figure 2, we evidence the bouncing to non-bouncing transition in the parameter space spanned by the Ohnesorge and Bond numbers for several fixed Weber numbers. We extract three key pieces of information from this regime map:

(i) The Weber number has a small influence on the transition between the bouncing and non-bouncing regime in the range probed in this study, $We = 1$–50, the same as

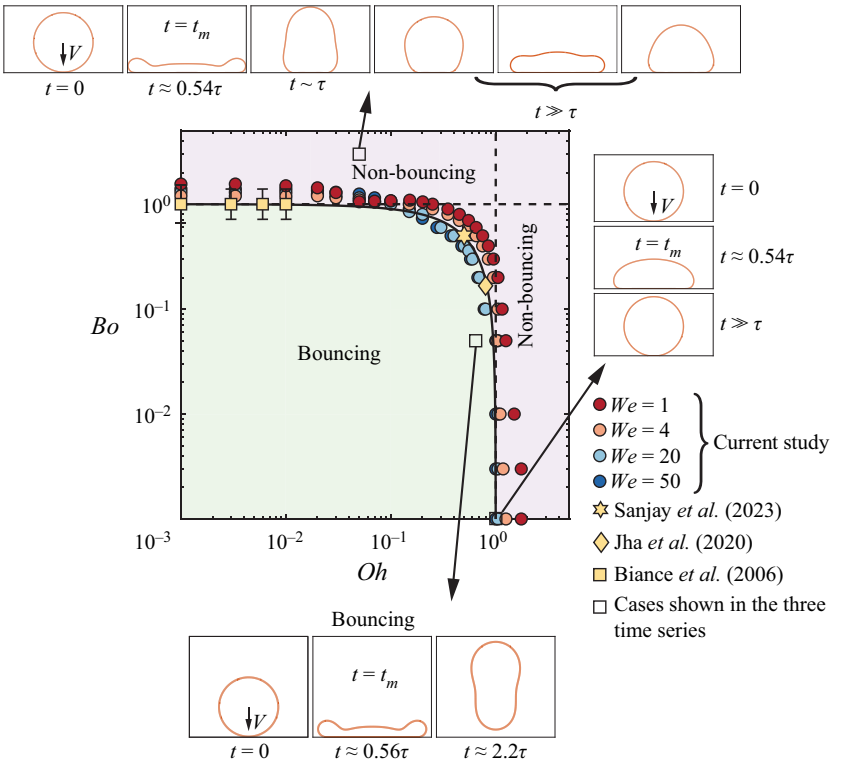

Figure 2. Regime map in terms of the Bond number $Bo = \rho_d g R^2/\gamma$ and the drop Ohnesorge number $Oh = \eta_d/\sqrt{\rho_d \gamma R}$, distinguishing the bouncing and non-bouncing regimes. The data points represent the transition between the bouncing and non-bouncing regimes at different Weber numbers We. The three series of insets illustrate typical cases in these regimes, namely $(We, Oh, Bo) = (16, 0.05, 3)$ for the upper, $(16, 1, 0.001)$ for the right and $(16, 0.75, 0.05)$ for the bottom series of images, respectively. The solid black line delineates the prediction of this transition ((3.6)). Lastly, the black dashed vertical and horizontal lines mark the two asymptotes, i.e. the viscous limiting case, $Oh_c = 1$ and the weight limiting case, $Bo_c = 1$, respectively. See also the supplementary movie SM1 available at https://doi.org/10.1017/jfm.2023.55.

what was reported by Jha *et al.* (2020) and Antonini *et al.* (2016) for the bouncing inhibition of viscous drops (see also Appendix B).

(ii) We recover the two limiting cases of non-bouncing (see insets of figure 2): drops smaller than their visco-capillary length, (i.e. $R < \eta_d^2/\rho_d\gamma$, giving $Oh > 1$) stop bouncing due to viscous dissipation (Jha *et al.* 2020), while those larger than their gravito-capillary length, (i.e. $R > \sqrt{\gamma/\rho_d g}$, giving $Bo > 1$) cannot bounce due to their weight (Biance *et al.* 2006). We will elaborate on the mechanisms of rebound inhibition in these two non-bouncing regimes in § 4.

(iii) Experiments performed with millimetre-sized drops of water or silicone oil do not lie on either asymptote (Jha *et al.* 2020; Sanjay *et al.* 2023), suggesting that both the effects of viscosity and gravity need to be taken into account to predict the bouncing to non-bouncing transition.

In this section, we focus on situations where bouncing is prevented by both viscous and gravitational effects (i.e. $Bo < 1$ and $Oh < 1$). Figure 3 shows snapshots illustrating three representative cases lying in this region of the parameter space for $We = 20$. Each snapshot displays three pieces of information: the position of the liquid–air interface, the

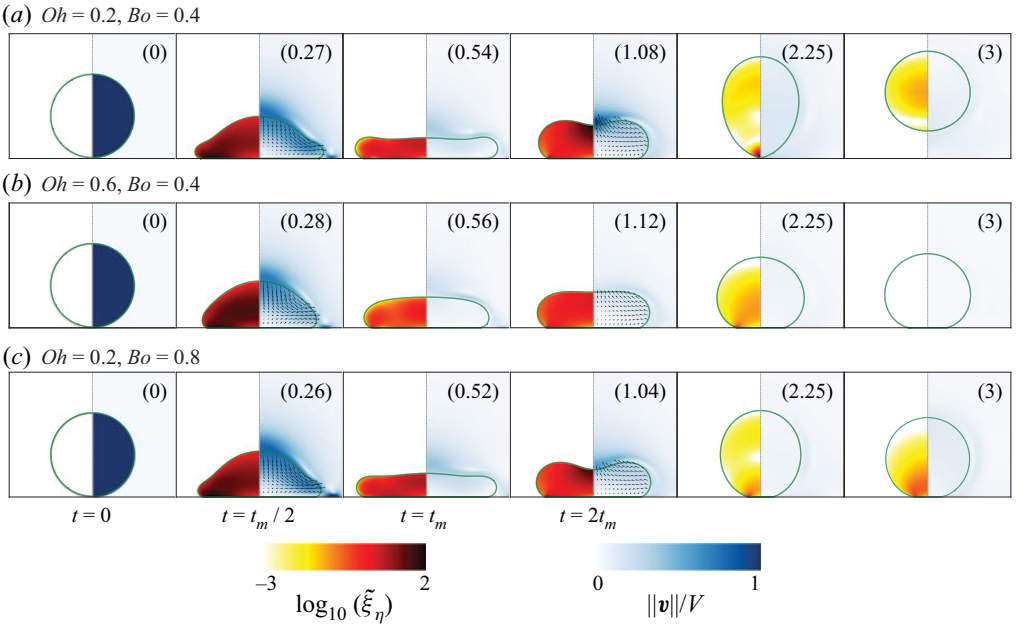

Figure 3. Direct numerical simulations snapshots illustrating the drop impact dynamics for (*a*) $(Oh, Bo) = (0.2, 0.4)$, (*b*) $(Oh, Bo) = (0.6, 0.4)$ and (*c*) $(Oh, Bo) = (0.2, 0.8)$. The left-hand side of each numerical snapshot shows the dimensionless viscous dissipation function $\tilde{\xi}_\eta = 2Oh(\tilde{\boldsymbol{\mathcal{D}}} : \tilde{\boldsymbol{\mathcal{D}}})$ on a $\log_{10}$ scale to identify regions of maximum dissipation (black). The right-hand side shows the magnitude of the velocity field normalised by the initial impact velocity, V. The black velocity vectors are plotted in the drop's centre of mass reference frame to evidence the internal flow. The numbers inside the bracket at right-top corner of each snapshot represent the dimensionless time, t/τ. For all cases, the impact Weber number is $We = 20$. See also the supplementary movie SM2.

dimensionless rate of viscous dissipation per unit volume (i.e. the dimensionless viscous dissipation function, left panel) and the magnitude of the velocity field normalised with the initial impact velocity (right panel). For $Oh = 0.2$ and $Bo = 0.4$ (figure 3*a*), the drop undergoes typical rebound dynamics. The liquid first spreads radially up to $t = t_m$, when the maximum extent is reached (Clanet *et al.* 2004; Eggers *et al.* 2010; Laan *et al.* 2014; Wildeman *et al.* 2016). This stage is followed by liquid retraction (Bartolo *et al.* 2005), parallel to the substrate, until the drop contracts ($t = 2t_m$) and the motion becomes vertical (Chantelot 2018; Zhang *et al.* 2022). Finally, the drop leaves the substrate at $t = 2.25\tau$ (Richard & Quéré 2000; Richard *et al.* 2002).

Surprisingly, increasing Oh to 0.6, below the critical value reported by Jha *et al.* (2020), while keeping $Bo = 0.4$ (figure 3*b*), prevents the rebound. The motion is damped before the drop can bounce off the substrate. Similarly, increasing Bo to 0.8, below the critical value reported by Biance *et al.* (2006), while fixing $Oh = 0.2$ (figure 3*c*), also inhibits bouncing. Yet, the deposited liquid undergoes multiple oscillation cycles on the substrate before coming to rest (see the last snapshot $t = 3\tau$).

In all three cases, the impact dynamics and flow in the drop are qualitatively similar until the maximum extent is reached at $t = t_m$. At this instant, the absence of internal flow suggests that the initial kinetic energy has either been converted into surface energy or lost to viscous dissipation, which occurs throughout the drop volume owing to $Oh \sim O(0.1)$ (Eggers *et al.* 2010). Close to the bouncing to non-bouncing transition, the rebound can

thus be understood as a process which converts an initial surface energy into kinetic energy, disentangling the later stages of the rebound from the initial impact dynamics.

This observation prompts us to introduce an analogy with coalescence-induced jumping, in which an excess surface energy, gained during coalescence, is converted into upward motion of the liquid (Boreyko & Chen 2009; Liu *et al.* 2014; Farokhirad *et al.* 2015). The spread drop, at rest at $t = t_m$, reduces its surface area through a Taylor–Culick-type retraction, converting excess surface energy into kinetic energy. The capillary force driving this radially inwards flow is

$$F_\gamma \sim \gamma R. \tag{3.1}$$

The velocity v associated with this Taylor–Culick-type retraction scales as $v \sim \sqrt{\gamma/(\rho_d e)}$, where e is the typical thickness of the spread liquid, which can be rearranged as $v \sim V_\gamma \sqrt{R/e}$ upon introducing the inertio-capillary velocity (Bartolo *et al.* 2005; Chantelot 2018). At the bouncing to non-bouncing transition, in the presence of both viscous and gravitational effects (see figure 2), we make the hypothesis that $e \sim R$, as no pronounced central film forms during spreading (see figure 3 at $t = t_m$), implying that the inertio-capillary velocity is the relevant velocity scale, i.e. $v \sim V_\gamma$. Similarly to the coalescence-induced jumping of two identical drops, a dissipative force $F_\eta \sim \Omega \eta_d \nabla^2 v$, where Ω is the volume of the drop and v is a typical radial flow velocity, opposes the capillarity driven flow (Mouterde *et al.* 2017*b*; Lecointre *et al.* 2019). Taking $v \sim V_\gamma$ as explained above, the resistive viscous force then scales as

$$F_\eta \sim \eta_d V_\gamma R, \tag{3.2}$$

and the effective momentum converging in the radial direction is

$$P_r \sim \int (F_\gamma - F_\eta)\, \mathrm{d}t. \tag{3.3}$$

The asymmetry originating from the presence of the substrate enables the conversion of the radially inward momentum to the upwards direction (figure 3, $t = 2t_m$). Following Mouterde *et al.* (2017*b*) and Lecointre *et al.* (2019), we assume that the vertical momentum scales with the radial one, i.e. $P_v \sim P_r$, allowing us to determine a criterion for the bouncing transition by balancing the rate of change of vertical momentum with the drop's weight F_g:

$$\frac{\mathrm{d}P_v}{\mathrm{d}t} = F_g \sim \rho_d R^3 g. \tag{3.4}$$

Using (3.1)–(3.3), we obtain

$$\gamma R - \eta_d V_\gamma R \sim \rho_d R^3 g. \tag{3.5}$$

Lastly, substituting $V_\gamma = \sqrt{\gamma/\rho_d R}$, and rearranging, we arrive at a criterion to determine the bouncing to non-bouncing transition as

$$Oh_c + Bo_c \sim 1, \tag{3.6}$$

where the subscript c stands for 'critical'. Equation (3.6), which is independent of the impact Weber number We, is the main result of the manuscript.

We test the criterion (3.6) for the bouncing to floating transition against data extracted from our direct numerical simulations and experiments from Biance *et al.* (2006), Jha *et al.* (2020) and Sanjay *et al.* (2023). In figure 2, the solid black line, representing (3.6) with prefactor 1, is in excellent quantitative agreement with the data when viscous and

gravitational effects inhibit bouncing, as well as in the two limiting regimes, $Oh_c \sim 1$ for $Bo \ll 1$ (Jha *et al.* 2020), and $Bo_c \sim 1$ for $Oh \ll 1$ (Biance *et al.* 2006) (black dotted lines).

In the next section, we focus on evidencing the physical mechanisms leading to bouncing suppression in each of the two limiting cases. But before this, we note that the data for different Weber numbers do not exactly collapse on the prediction of (3.6), suggesting that the critical Ohnesorge and Bond numbers vary weakly with the Weber number, and hinting at the limitations of our hypothesis in choosing V_γ as the velocity scale, and neglecting the influence of *We* on the retraction velocity.

4. Limiting cases

4.1. *How does a viscous drop stop bouncing?*

We first investigate how viscous drops, much smaller than their gravito-capillary length, i.e. with $Bo \ll 1$, stop bouncing. We study this regime, in which the transition criterion (3.6) reduces to $Oh_c \sim 1$, by setting *Bo* to 0 (i.e. by assuming that capillarity dominates over gravity) and by systematically varying the drop Ohnesorge number, *Oh*. We characterise the rebound behaviour by measuring the apparent contact time t_c between the drop and the substrate and the coefficient of restitution ε, that we define as $\varepsilon = v_{cm}(t_c)/V$, where $v_{cm}(t_c)$ is the centre of mass velocity at take-off. The procedure used to extract t_c and ε from the direct numerical simulations is detailed in Appendix A.

In figure 4, we plot the coefficient of restitution ε and the normalised contact time t_c/τ as a function of *Oh* for Weber numbers ranging from 1 to 50. The effect of *Oh* on ε and t_c is markedly different. On the one hand, the coefficient of restitution monotonically decreases from its low *Oh*, Weber-dependent value

$$\varepsilon_0(We) = \varepsilon(We, Oh \to 0, Bo = 0), \tag{4.1}$$

with increasing *Oh*, until a critical Ohnesorge number of order one, Oh_c, marking the end of the bouncing regime. On the other hand, increasing *Oh* by over two orders of magnitude hardly affects t_c. It keeps its Weber-independent value $\tau_0 = 2.25\tau$, expected from the inertio-capillary scaling in the low *Oh* limit (Wachters & Westerling 1966; Richard *et al.* 2002), until t_c diverges as *Oh* tends towards Oh_c.

Figure 4 also highlights that Oh_c varies weakly with *We* ($Oh_c = 1.75, 1.5, 1, 1$ at $We = 1, 4, 20, 50$, respectively, see inset of figure 4*b*) as evidenced by the narrow grey shaded region, and in agreement with the limit predicted from (3.6). Varying *We* mainly affects the low *Oh* restitution limit $\varepsilon_0(We)$, which we elaborate on in Appendix B. We stress that the weak variation of the coefficient of restitution in the shaded region, where $\varepsilon < 0.1$, could go unnoticed in typical side view experiments. Indeed, $\varepsilon = 0.1$ corresponds to a centre of mass rebound height of 0.01 times the initial impact height, that is 10 μm for $We = 1$.

We now seek to understand the evolution of the restitution coefficient ε with *Oh* by quantifying the overall energy budget during an impact event. In the $Bo = 0$ limit, the energy balance reads

$$\tilde{E}_0 = \tilde{E}_k(\tilde{t}) + \Delta\tilde{E}_\gamma(\tilde{t}) + \tilde{E}_\eta(\tilde{t}), \tag{4.2}$$

where each energy component is normalised using the capillary energy scale γR^2, E_0 denotes the drop's initial kinetic energy, ($\tilde{E}_0 = E_0/(\gamma R^2) = (2\pi/3)We$), $E_k(t)$ and $E_\gamma(t)$ are the drop's time-dependent kinetic and surface energies, with $\Delta E_\gamma(t) = E_\gamma(t) - E_\gamma(t=0)$, and $E_\eta(t)$ is the viscous dissipation until time t. Readers are referred to Landau

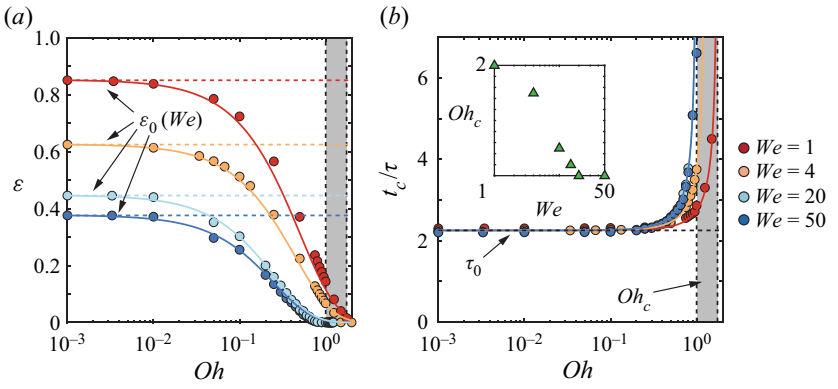

Figure 4. Variation of (*a*) the restitution coefficient ε, and (*b*) the contact time t_c, normalised by the inertio-capillary time scale $\tau = \sqrt{\rho_d R^3/\gamma}$, with the drop Ohnesorge number Oh for $Bo = 0$ at different Weber numbers We. In both panels, the solid lines represent the predictions of the spring–mass–damper system of Jha *et al.* (2020) (contact time, (4.3) and restitution coefficient, (4.4)). The horizontal dashed lines represent the contact time and restitution coefficient values in the $Oh \ll 1$ limit, in which $\tau_0 = 2.25\tau$, independent of We, while $\varepsilon_0(We) = \varepsilon(We, Oh \to 0, Bo = 0)$ (4.1) depends on We. Lastly, the black vertical lines and the grey shaded regions mark the critical Ohnesorge number $Oh_c \sim O(1)$ beyond which drops do not bounce.

& Lifshitz (1987), Wildeman *et al.* (2016), Ramírez-Soto *et al.* (2020), Sanjay *et al.* (2022) and Sanjay (2022*b*) for details of energy budget calculations.

Figure 5(*a*) evidences the time evolution of the energy balance contributions for an impact with $We = 1$ and $Oh = 0.001$. The drop's initial kinetic energy E_0 is transferred into surface energy until the liquid reaches its maximal extent at $t = t_m$ (note that for $We = 1$, $t_m \approx \tau$, see Zhang *et al.* 2022). At this instant, the energy available to the drop is almost exclusively stored in the form of excess surface energy, as hypothesised in our analogy with coalescence-induced jumping. As the drop retracts, surface energy is converted back into kinetic energy and, at take-off, the drop recovers a large proportion of its initial kinetic energy, $E_k(t_c) \approx 0.75E_0$. Energy dissipation throughout the rebound, $E_\eta(t_c)$, and the non-spherical drop shape at take-off, storing excess surface energy $\Delta E_\gamma(t_c)$, hamper the recovery of the initial kinetic energy. Even in the low We and low Oh case at hand, where dissipation is restricted to the boundary layer at the drop–air interface and happens due to the propagation of capillary waves (see the insets of figure 5(*a*) and Renardy *et al.* 2003; Zhang *et al.* 2022), viscous stresses dissipate 20% of the initial energy during the rebound.

Increasing the drop Ohnesorge number to $Oh = 2$ does not affect the energy transfer dynamics (figure 5*b*), but it enhances viscous dissipation, which now takes place in the whole liquid volume (see the insets of figure 5(*b*) and Eggers *et al.* 2010). Beyond the critical Ohnesorge number Oh_c, the initial kinetic energy is dissipated before the drop can rebound off the substrate. The drop impact process becomes over-damped and, in this small Bond number limit, the drop slowly relaxes back to its sessile spherical shape (figure 5*b*).

Figures 5(*c*) and (*d*) summarise the distribution of energy at take-off as a function of Oh for $We = 1$ and $We = 20$, respectively. For $Oh < 0.01$, the overall energy budget is not affected by a change in drop Ohnesorge number, extending the validity domain of the so-called inviscid drop limit (Richard & Quéré 2000). Strikingly, the independence of $E_\eta(t_c)$, and thus of ε, with Oh in this limit does not imply that viscous dissipation is negligible. Indeed, (i) the dissipated energy accounts for more than two thirds of the total kinetic energy loss during impact at $We = 1$, where the restitution is maximal, and

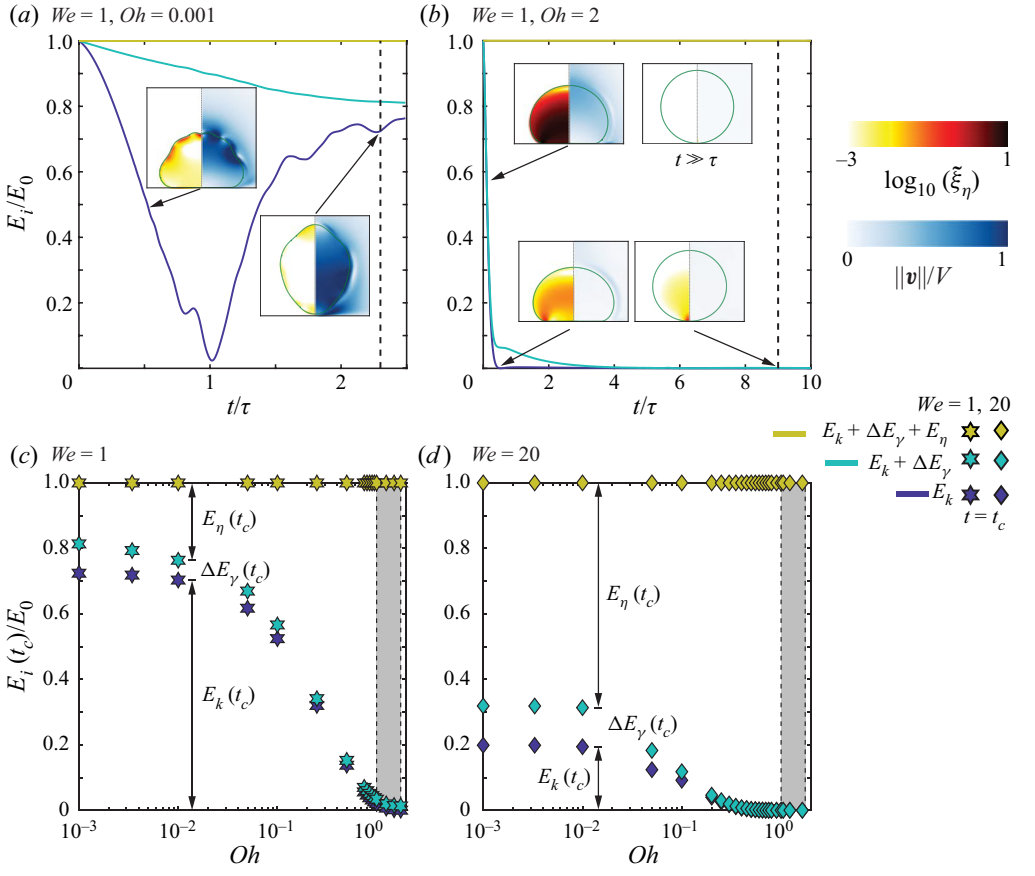

Figure 5. Energy budgets for drop impacts with $Bo = 0$ and $We = 1$ for (*a*) $Oh = 0.001$ and (*b*) $Oh = 2$. Here, E_k and E_η represent the kinetic energy and viscous dissipation, respectively, ΔE_γ denotes the change in surface energy with its zero set at $t = 0$. The numerical snapshots in the insets illustrate the drop morphologies and the anatomy of the flow with a colour code identical to that of figure 3. The black dotted lines in panels (*a*) and (*b*) mark the instant t_c when the drop takes off and when the normal contact force between the drop and the substrate is minimum, respectively. (*c*,*d*) Energy distributions at $t = t_c$ for $We = 1$ (*c*) and $We = 20$ (*d*) as function of Oh. The black vertical lines and the grey shaded regions mark the critical Ohnesorge number $Oh_c \sim O(1)$ beyond which drops do not bounce. See also supplementary movie SM3.

(ii) the increase of viscous dissipation is mainly responsible for the decrease of ε with We. The dissipated energy $E_\eta(t_c)$ accounts for 20 % and 70 % of E_0 for $We = 1$ and $We = 20$, respectively, contradicting the inviscid nature of this regime. The transfer of the initial kinetic energy into surface energy $\Delta E_\gamma(t_c)$ at take-off, that is the rebound of the liquid in a non-spherical shape, while accounting for one third the total energy loss during impact at $We = 1$, cannot alone explain the significantly lower than one value of the coefficient of restitution.

The presence of a finite energy dissipation in the limit $Oh \to 0$ is reminiscent of the dissipative anomaly in fully developed turbulence, expressing that, even in the limit of vanishing viscosity (i.e. diverging Reynolds number $Re \to \infty$), the energy dissipation rate remains finite (Kolmogorov 1941; Onsager 1949; Eyink 1994; Eggers 2018; Dubrulle 2019). The dissipative anomaly reflects in the finite drag experienced by solid bodies at diverging Reynolds numbers, through the creation of boundary layers (Prandtl 1904),

somewhat similar to the localisation of viscous dissipation at the liquid–air interface during drop impact (see the inset of figure 5(*a*) and Philippi *et al.* 2016).

For larger Ohnesorge numbers, the dissipated energy $E_\eta(t_c)$ increases with Oh, reflecting that viscous dissipation is responsible for the loss of the rebound elasticity. Interestingly, increasing Oh also reduces the drop deformation at take-off, decreasing the fraction of energy stored as surface energy $\Delta E_\gamma(t_c)$. Consequently, energy which is not lost to viscous dissipation is mainly converted back into the kinetic energy of the drop, leading to a more efficient recovery of the initial kinetic energy (figure 5*c*,*d*).

We further rationalise our observations by comparing our simulation results with the predictions of Jha *et al.* (2020) that extend the liquid spring analogy to viscous drops. This minimal model, that has been shown to successfully capture the variation of t_c and ε with Oh, gives the time of apparent contact as

$$t_c(We, Oh, Bo = 0) = \tau_0 \left(\frac{1}{\sqrt{1 - (Oh/Oh_c(We))^2}} \right), \tag{4.3}$$

which is in quantitative agreement with our simulation data (figure 4*b*) when the critical Ohnesorge number $Oh_c(We)$ at which bouncing stops is taken from the simulations (see the inset of figure 4*b*). Jha *et al.* (2020) also predict the coefficient of restitution, written in our notations as

$$\varepsilon(We, Oh, Bo = 0) = \varepsilon_0(We) \exp\left(\frac{-\beta Oh/Oh_c(We)}{\sqrt{1 - (Oh/Oh_c(We))^2}} \right), \tag{4.4}$$

where β is an adjustable We-independent parameter. The simulation data and the model are in excellent agreement for $\beta = 4.00 \pm 0.25$ (figure 4*a*). Note that Jha *et al.* (2020) further reduced (4.4) to $\varepsilon(We, Oh, Bo = 0) \approx \varepsilon_0(We) \exp(-\alpha Oh)$ for $Oh \ll Oh_c$, where $\alpha = \beta/Oh_c = 2.5 \pm 0.5$ best fits the experimental data, independent of the impact Weber number. The equivalent fitting parameter for our case is $\alpha' = \beta'/Oh_c = 3 \pm 1$, in very good agreement with the value reported by Jha *et al.* (2020), despite the different Bond number ($Bo = 0$ here vs. $Bo = 0.167$ for Jha *et al.* (2020), also see § 4.2 and Appendix B).

Finally, we discuss the failure of the model of Jha *et al.* (2020) to predict the low Oh behaviour of the coefficient of restitution that is contained in the prefactor ε_0. The analysis of the overall energy budget shows that two ingredients are responsible for the loss of the initial drop kinetic energy in the $Oh < 0.01$ limit: (i) the presence of excess surface energy at take-off $\Delta E_\gamma(t_c)$ and (ii) the viscous dissipation in thin boundary layers at the liquid–air interface. Both these contributions are not accounted for in the model of Jha *et al.* (2020) which takes no deformation, i.e. $\Delta E_\gamma(t_c) = 0$ as a take-off condition, and $\eta_d VR$ as the scaling form of the viscous damping term, added to the liquid spring, which supposes that dissipation occurs at the drop length scale. However, as Oh increases, bulk dissipation becomes dominant, explaining the ability of the model to capture bouncing inhibition.

4.2. *How does a heavy drop stop bouncing?*

We now discuss the rebound inhibition of heavy drops, much larger than than their visco-capillary lengths, i.e. with $Oh \ll 1$. We study this limit, in which (3.6) reduces to $Bo_c \sim 1$, by fixing $Oh = 0.01$, in the so-called inviscid bouncing regime (figures 4 and 5), and by varying the Bond number Bo.

In figure 6, we show the evolution of the coefficient of restitution ε and of the normalised contact time t_c/τ as a function of the Bond number Bo for four values of

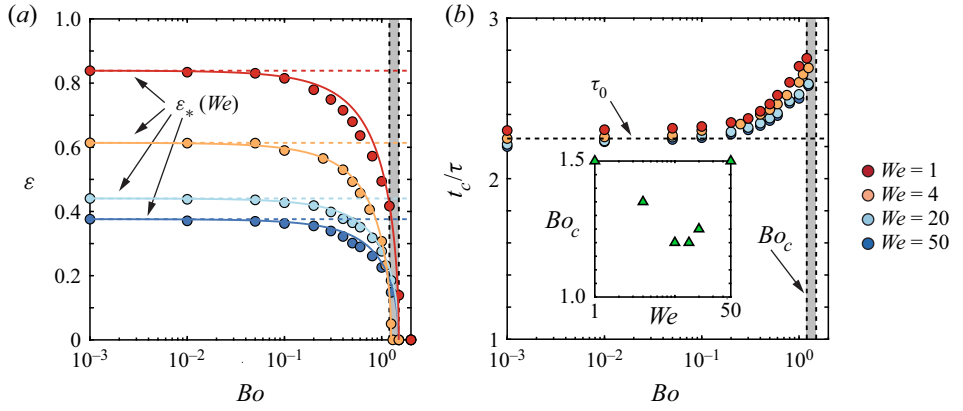

Figure 6. Variation of (*a*) the restitution coefficient ε, and (*b*) the contact time t_c, normalised by the inertio-capillary time scale $\tau = \sqrt{\rho_d R^3/\gamma}$, with the Bond number Bo at different Weber numbers We in the so-called inviscid regime ($Oh = 0.01$). In panel (*b*), the solid lines represent the predictions of the model of Biance *et al.* (2006), see (4.6). The horizontal dashed lines represent the contact time and restitution coefficient values in the limit of zero Bond number ($\varepsilon(We, Oh = 0.01, Bo = 0)$), while the black vertical lines and the grey shaded regions mark the critical Bond number $Bo_c \sim O(1)$ beyond which drops do not bounce. Note that the model of Biance *et al.* (2006) predicts a constant t_c (horizontal dashed line in panel *a*), in contradiction to our numerical simulations.

the Weber number. The variation of ε with Bo is qualitatively similar to that observed when sweeping across the viscous drop asymptote. The coefficient of restitution ε slowly decreases from its Weber-dependent value $\varepsilon_*(We) = \varepsilon(We, Oh = 0.01, Bo = 0)$ with increasing Bond number, until it approaches a critical Bond number Bo_c, of order one, at which it sharply decreases to zero. Here, in the so-called inviscid regime, $\varepsilon_*(We) \approx \varepsilon_0(We)$. However, the influences of Bo and Oh on t_c are different. The contact time value hardly deviates from its inertio-capillary value, $\tau_0 = 2.25\tau$, when varying Bo over two orders of magnitude. Yet, we only observe a moderate increase of t_c as Bo_c is approached, contrasting with the divergence of t_c close to Oh_c.

Figure 6 also evidences that varying the Weber number We from 1 to 50 hardly affects the critical Bond number Bo_c (see the inset of figure 6*b*), marking the transition from bouncing to floating, as underlined by the grey shaded regions and in agreement with the transition criterion (3.6). Similarly as for viscous drops, increasing We does not influence the contact time but markedly decreases ε_*, an effect we quantify in Appendix B.

To further investigate the variation of ε with Bo, we compute the overall energy budget during an impact event. In the presence of gravity, the energy balance (4.2) incorporates an additional contribution from the drop's gravitational potential energy, ΔE_g, whose zero is set at the instant of maximum drop deformation. The modified energy balance reads

$$\tilde{E}_0 = \tilde{E}_k(\tilde{t}) + \Delta\tilde{E}_g(\tilde{t}) + \Delta\tilde{E}_\gamma(\tilde{t}) + \tilde{E}_\eta(\tilde{t}), \tag{4.5}$$

where the initial energy also includes gravity, $\tilde{E}_0 = (4\pi/3)(We/2 + Bo(1 - \mathcal{H}))$, with $\mathcal{H}$ denoting the centre of mass height of the drop at maximum deformation.

Figure 7(*a*) illustrates the energy budget for $(We, Oh, Bo) = (1, 0.01, 0)$. The energy transfer follows a similar dynamics as that described in figure 5(*a*), where $(We, Oh, Bo) = (1, 0.001, 0)$. The fraction of the initial kinetic energy recovered at take-off is the same, $E_k(t_c) \approx 0.75E_0$. We also note that, although Oh has increased by an order of magnitude compared with the case shown in figure 5(*a*), the energy lost to viscous dissipation still accounts for a similar fraction of the initial energy, $E_\eta(t_c) \approx 0.2E_0$, as expected in the

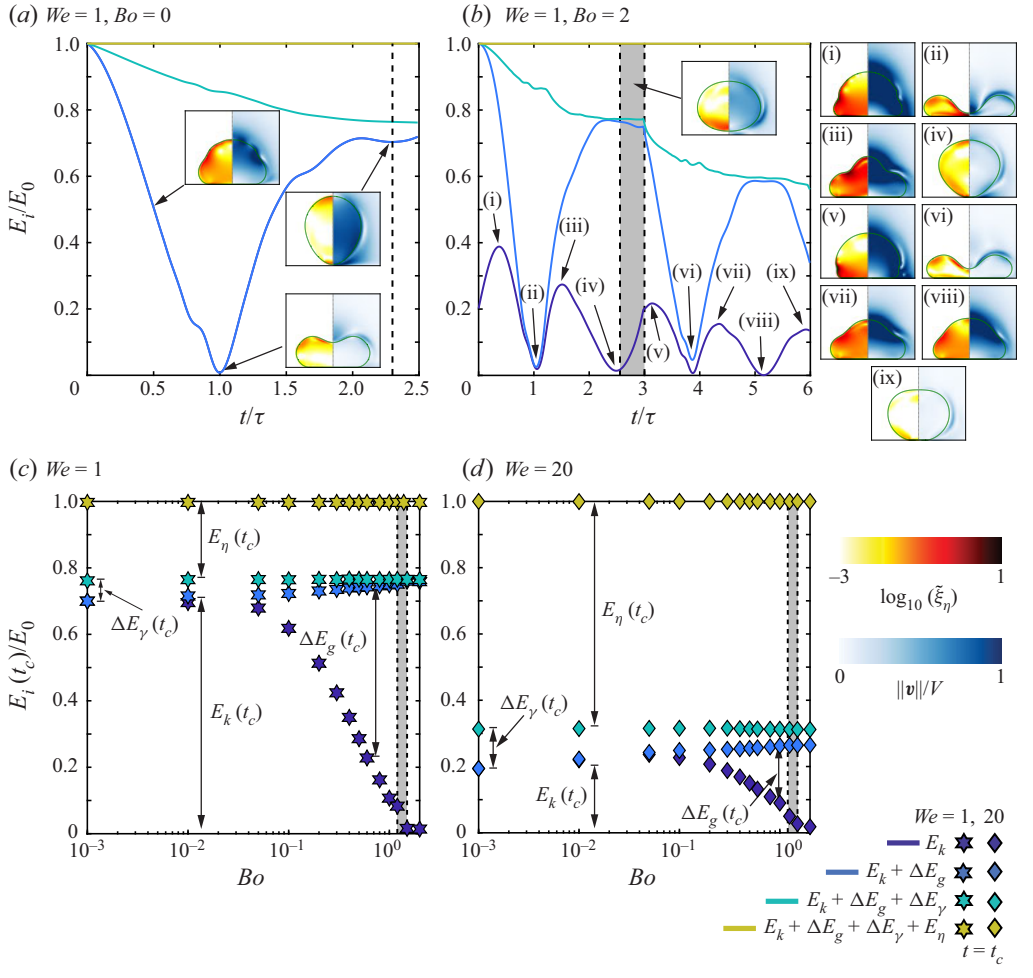

Figure 7. Energy budgets for drop impacts with $Oh = 0.01$ and $We = 1$ for $Bo = 0$ (*a*) and $Bo = 2$ (*b*). Here, E_k and E_η represent the kinetic energy and viscous dissipation, respectively, ΔE_g and ΔE_γ denote the the change in gravitational potential energy and surface energy with their zeros set at the instant of maximum spreading of the impacting drop, and at $t = 0$, respectively. The numerical snapshots in the insets illustrate the drop morphologies and the anatomy of the internal flow with a colour code identical to that of figure 3. The vertical dotted line in panel (*a*) marks the instant when the drop takes off. In panel (*b*), the black vertical lines and the grey shaded regions bounds the time interval when the normal contact force between the drop and the substrate is zero. (*c*,*d*) Energy distributions at $t = t_c$ for $We = 1$ (*c*) and $We = 20$ (*d*) as a function of Bo. For non-bouncing cases, t_c represents the end of first drop oscillation cycle. The black vertical lines and the grey shaded regions in panels (*c*) and (*d*) mark the critical Bond number $Bo_c \sim O(1)$ beyond which drops do not bounce. See also supplementary movie SM4.

so-called inviscid drop limit. The snapshots of the drop's internal flow (see the insets of figures 5*a* and 7*a*) give insight into the independence of $E_\eta(t_c)$ with Oh. As the drop Ohnesorge number is increased, two antagonistic effects take place: (i) the viscous boundary layer grows larger, increasing dissipation, and (ii) capillary waves are attenuated, decreasing local dissipation. This competition qualitatively explains the independence of $E_\eta(t_c)$ and ε on the drop Ohnesorge number for $Oh < 0.01$.

Increasing the Bond number to $Bo = 2$, beyond Bo_c, sheds light on the mechanism of bouncing inhibition of heavy drops. At $t = 0$, the drop has a higher initial energy owing

to the contribution from the gravitational potential energy. As a result, the kinetic energy E_k increases until the inertial shock is propagated throughout the drop (see figure 7*b*-i and Gordillo *et al.* 2018; Cheng, Sun & Gordillo 2021), before decreasing and reaching a minimum as the drop then attains maximum deformation (figure 7*b*-ii). In spite of these differences, the maximal spreading time is the same as that observed at low Bo, $t_m \approx \tau$ (for $We = 1$, see Zhang *et al.* 2022), and viscous dissipation enervates a similar proportion of the initial energy as in the low Bo case during spreading. During the retraction stage, E_k increases (figures 7*b*-ii to 7*b*-iii), until the motion goes from being dominantly in the radial direction to being dominantly in the axial direction (figure 7*b*-iii, $t \approx 1.5\tau$, see Chantelot 2018; Zhang *et al.* 2022). Beyond this instant, gravity opposes the upward motion of the drop, E_k decreases and is mainly transferred to E_g until, eventually, at $t \approx 2.5\tau$ (figure 7*b*-iv) the drop's centre of mass starts moving in the downward direction. At this instant, only 20 % of the drop's initial energy goes to viscous dissipation, identical to the case of $Bo = 0$, but bouncing is inhibited. In contrast to the viscous asymptote, energy is still available to the drop even though the rebound is suppressed. Subsequently, the drop undergoes several capillary oscillations at the substrate with a time period of approximately 2.5τ (figures 7*b*-v to 7*b*-ix).

Figures 7(*c*) and 7(*d*) show the distribution of energy at take-off as a function of Bo for $We = 1$ and $We = 20$, respectively. For both Weber numbers, as Bo increases, the fraction of initial energy that goes into viscous dissipation, $E_\eta(t_c)$, is constant. However, the gravitational potential energy $\Delta E_g(t_c)$, initially negligible for $Bo = 0.001$, increases with increasing Bo, leading to a decrease of the drop's kinetic energy at take-off $E_k(t_c)$, which eventually drops to zero as bouncing stops at Bo_c. Noticing that energy is still available to the drop in the form of gravitational potential energy at $t = t_c$ allows us to rationalise the different behaviour of t_c with Bo and Oh. Indeed, the viscous rebound suppression corresponds to a transition from an underdamped to an overdamped system, associated with a divergence of the oscillation period, while heavy drops undergo successive energy transfers between gravitational potential, kinetic and surface energy on the inertio-capillary time scale.

Finally, we compare the variation of ε and t_c with Bo extracted from our simulations to the spring–mass model of Biance *et al.* (2006) which takes into account the role of gravity but neglects viscous dissipation. In our notation, the dependence of ε on Bo in the model of Biance *et al.* (2006) is written as

$$\varepsilon(We, Oh = 0.01, Bo) = \varepsilon_*(We)\sqrt{(1 - Bo/Bo_c(We))(1 + Bo/(3Bo_c(We)))}. \tag{4.6}$$

Equation (4.6) is in excellent quantitative agreement with the values of $\varepsilon_*(We)$ and $Bo_c(We)$ extracted from the simulations (figure 6*a*). However, this model predicts a constant t_c which is in disagreement with our simulations as we approach Bo_c (figure 6*b*). We further stress that the model of Biance *et al.* (2006), similarly to that of Jha *et al.* (2020), does not capture the evolution of the prefactor ε_* or ε_0 with We. It indeed does not take into account viscous dissipation, which we have shown to be the main ingredient responsible for the loss of rebound elasticity as We is increased. We address the relevance of this model in predicting the variation of the coefficient of restitution with We in Appendix B.

5. Conclusion and outlook

Drops smaller than their visco-capillary length, i.e. with $Oh > 1$, stop bouncing due to viscous dissipation, while those larger than their gravito-capillary length, i.e. with $Bo > 1$, cannot bounce due to their weight. In this paper, we investigate how viscous stresses

and gravity oppose capillarity to prevent drops of intermediate sizes, with $\eta_d^2/\rho_d\gamma < R < \sqrt{\gamma/\rho_d g}$, corresponding to $Bo < 1$ and $Oh < 1$, from bouncing off non-wetting substrates. We emphasise the relevance of this regime, which describes the bouncing inhibition of millimetre-sized aqueous or silicone oil drops, commonly used in experiments. Drawing an analogy with coalescence-induced jumping of two identical drops, we propose the criterion $Oh_c + Bo_c \sim 1$ for the bouncing to non-bouncing transition. Through a series of direct numerical simulations, we show the validity of this criterion over a wide range of Weber numbers in the *Bo*–*Oh* phase space.

We also study the details of the mechanism of rebound suppression in the two limiting cases of low drop Ohnesorge number and Bond number, by relating the overall energy budget to the drop morphology and flow anatomy. For drops much smaller than their gravito-capillary lengths ($Bo \ll 1$), simulations confirm that the increase of viscous dissipation in the bulk of the liquid is responsible for rebound suppression. The restitution coefficient decays exponentially with increasing Oh until a critical Ohnesorge number Oh_c, of order one, is reached and the contact time diverges as the rebound process becomes over-damped. This behaviour is well captured by the model of Jha *et al.* (2020) which extends the spring–mass analogy to viscous drops by including bulk viscous dissipation in the liquid. Moreover, the energy budgets reveal that the rebound elasticity in the so-called inviscid regime $Oh < 0.01$, in which the restitution coefficient is independent of Oh, is controlled by viscous dissipation occurring in thin boundary layers, shedding light on the failure of simple scaling models to capture this regime. We also evidence that the decrease of rebound elasticity with increasing *We* in the so-called inviscid regime is a consequence of enhanced viscous dissipation, as the surface energy stored at take-off plays a negligible role in setting ε.

For drops much larger than their visco-capillary lengths ($Oh \ll 1$), the excess gravitational potential energy at take-off stops the drop from rebounding when the Bond number reaches a critical value Bo_c, of order one. Indeed, an increase in *Bo* does not change the fraction of the drop initial energy that goes into viscous dissipation during the impact process. The restitution coefficient deviates slowly from its *We*-dependent value at zero Bond number, until it decreases sharply to zero as Bo_c is reached. This decrease is quantitatively captured by the spring–mass model of Biance *et al.* (2006), which takes into account the effect of gravity. We stress that, as the rebound is suppressed, energy is still available to the drop which subsequently oscillates on the substrate on the inertio-capillary time scale. Contrary to viscous bouncing inhibition, the rebound suppression of heavy drops is not associated with a divergence of the contact time.

Finally, we emphasise that this work describes the upper bound of the bouncing to non-bouncing transition on ideal non-wetting substrates. Indeed, water drops can cease bouncing due to substrate pinning on superhydrophobic substrates (Sarma, Dalal & Basu 2022). We also idealised the role of the surrounding medium by keeping a small value for the Ohnesorge number, $Oh_a = 10^{-5}$. We anticipate that dissipation in the surrounding medium might play a role in the impact of microdrops as Oh_a increases (Kolinski, Mahadevan & Rubinstein 2014; Tai *et al.* 2021). Lastly, the influence of the Weber number on the elasticity of the impact process deserves further investigation. Here, we only focus on impacts with $We \geq 1$, where the bouncing inhibition and drop contact time are reasonably insensitive to an increase in Weber number. Yet, modelling the full Weber number dependence of the restitution coefficient at both low *Oh* and low *Bo* still demands further work. It will be particularly interesting to study the regime $We \ll 1$, where drops only deform weakly, and the internal flow is still significant at the instant of maximum spreading.

Supplementary material. Supplementary movies are available at https://doi.org/10.1017/jfm.2023.55. The codes used in the present article are permanently available on GitHub (Sanjay 2022*a*).

Acknowledgements. We thank A. Jha for sharing data and for stimulating discussions. We also thank U. Sen, M. Jalaal, A. Prosperetti, D. Quéré and J. Snoeijer for discussions. We acknowledge S. Lakshman for preliminary experiments that made us numerically and theoretically explore the effect of gravity in viscous drop bouncing. This work was carried out on the national e-infrastructure of SURFsara, a subsidiary of SURF cooperation, the collaborative ICT organisation for Dutch education and research.

Funding. The authors acknowledge the ERC Advanced Grant No. 740479-DDD.

Declaration of interests. The authors report no conflict of interest.

Author ORCIDs.
Vatsal Sanjay https://orcid.org/0000-0002-4293-6099;
Pierre Chantelot https://orcid.org/0000-0003-1342-2539;
Detlef Lohse https://orcid.org/0000-0003-4138-2255.

Appendix A. Measuring the restitution coefficient

Throughout this manuscript, we have used the time of contact and restitution coefficient to study the drop impact dynamics. In this appendix, we describe the procedure used to determine the restitution coefficient which is the ratio of take-off velocity $v_{cm}(t_c)$ to the impact velocity V:

$$\varepsilon = \frac{v_{cm}(t_c)}{V}, \tag{A1}$$

where t_c denotes the contact time when the drop leaves the substrate. We assume an ideal non-wetting substrate by ensuring that a thin air layer (with a minimum thickness of $\Delta = R/1024$, where Δ is the minimum grid size employed in the simulations) is always present between the drop and the substrate (also see Ramírez-Soto *et al.* 2020). Hence, we need to define a criterion for the end of contact. We do so at the instant when the normal reaction force F between the substrate and the drop is zero (for calculation details, see Zhang *et al.* 2022), as shown in figure 8(*a*). Subsequently, we read out the centre of mass velocity (figure 8*b*) at this instant. If this centre of mass velocity is not in the upward direction (i.e. it is zero or negative), we categorise the case as non-bouncing. For the representative case in figure 8, $\varepsilon = 0.47$.

Appendix B. Influence of Weber number

We report that the bouncing inhibition and drop contact time are fairly insensitive to an increase in the impact Weber number (We) while the restitution coefficient decreases monotonically with We. Figure 9 illustrates the variation of the restitution coefficient with We at different Oh and fixed $Bo = 0.167$, enabling comparison with the experimental data of Jha *et al.* (2020). In the so-called inviscid drop limit ($Oh \lesssim 0.01$), the coefficient of restitution is approximately equal to the prefactors $\varepsilon_0(We)$ and $\varepsilon_*(We)$ used in § 4, (4.4) and (4.6), respectively.

For $Oh \lesssim 0.01$, ε does not follow the $1/\sqrt{We}$ scaling relation derived by Biance *et al.* (2006) using a spring–mass model that neglects the influence of the drop viscosity. Indeed, the energy budgets reported in figures 5(*c*,*d*) and 7(*c*,*d*) evidence that the transfer to surface energy at take-off $\Delta E_\gamma(t_c)$, proposed by Biance *et al.* (2006) to account for the loss of rebound elasticity, negligibly contributes to the decrease of ε with We. Instead, we find that

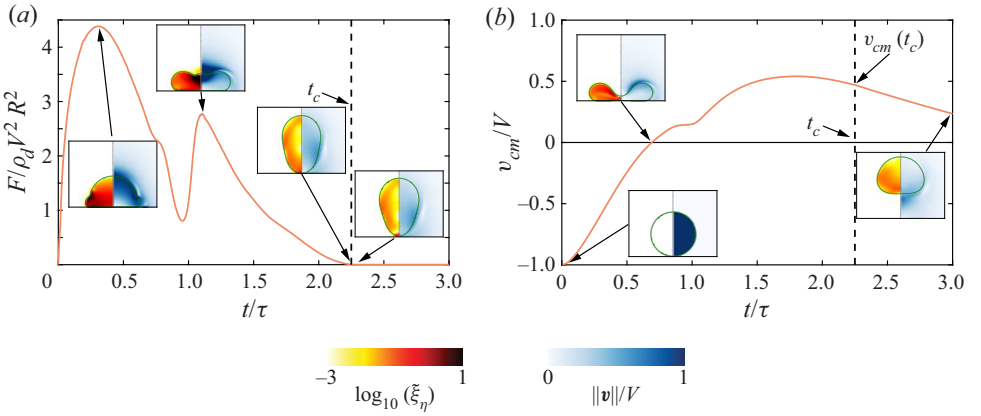

Figure 8. A representative temporal variation of (*a*) the normal reaction force F on the drop and (*b*) its centre of mass velocity v_{cm}. Time is normalised using the inertio-capillary time scale τ. Insets illustrate the different stages of the drop impact process. The background shows the magnitude of the rate of viscous dissipation per unit volume ($\tilde{\xi}_\eta = 2Oh(\tilde{\mathcal{D}} : \tilde{\mathcal{D}})$) on the left and the magnitude of velocity field normalised by the impact velocity on the right. The vertical dashed black line represents the contact time calculated using the criterion $F = 0$, marking the end of contact between the drop and the substrate. Here, $(We, Oh, Bo) = (4, 0.034, 0.5)$, the contact time $t_c = 2.25\tau$ and the coefficient of restitution $\varepsilon = 0.47$.

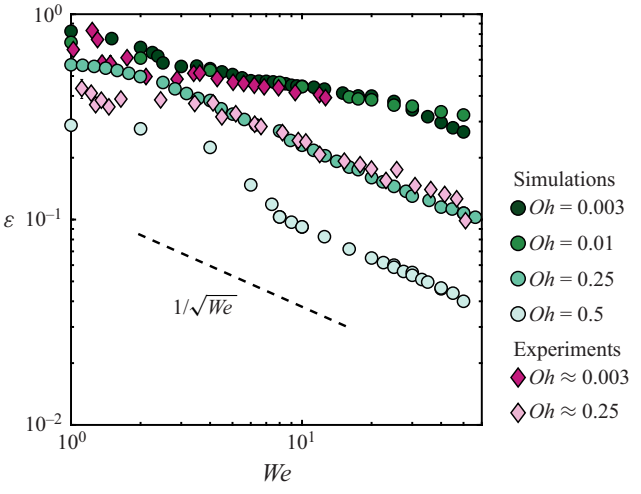

Figure 9. Variation of the restitution coefficient with the impact Weber number (*We*) at different drop Ohnesorge numbers (*Oh*). The simulations (circle data points) match perfectly with the experimental results (diamond data points) of Jha *et al.* (2020) without any fitting parameters. Here, the Bond number (*Bo*) is 0.167.

the increase of viscous dissipation with *We* drives the decrease of ε, even in the so-called inviscid limit.

Interestingly, the restitution coefficient for viscous drop impacts ($Oh \gtrsim 0.1$) seems to follow the $1/\sqrt{We}$ scaling relation, implying that the take-off velocity scales with the Taylor–Culick-type velocity ($v_{cm}(t_c) \sim \sqrt{\gamma/\rho_d R}$), and is independent of the impact velocity V, consistent with our assumption that the retraction and take-off stages are independent of the impact Weber number. We caution here that the range of *We* ($1 \leq We \leq 50$) is too small to claim this scaling relation convincingly.

Lastly, notice the remarkable agreement between our simulations and the experimental data points from Jha *et al.* (2020) for two different drop Ohnesorge numbers, which differ by over two orders of magnitude (see figure 9).

References

Antonini, C., Jung, S., Wetzel, A., Heer, E., Schoch, P., Moqaddam, A.M., Chikatamarla, S.S., Karlin, I., Marengo, M. & Poulikakos, D. 2016 Contactless prompt tumbling rebound of drops from a sublimating slope. *Phys. Rev. Fluids* **1** (1), 013903.

Bartolo, D., Josserand, C. & Bonn, D. 2005 Retraction dynamics of aqueous drops upon impact on non-wetting surfaces. *J. Fluid Mech.* **545**, 329–338.

Bergeron, V., Bonn, D., Martin, J.Y. & Vovelle, L. 2000 Controlling droplet deposition with polymer additives. *Nature* **405** (6788), 772–775.

Biance, A.L., Chevy, F., Clanet, C., Lagubeau, G. & Quéré, D. 2006 On the elasticity of an inertial liquid shock. *J. Fluid Mech.* **554**, 47–66.

Blossey, R. 2003 Self-cleaning surfaces–virtual realities. *Nat. Mater.* **2** (5), 301–306.

Boreyko, J.B. & Chen, C.H. 2009 Self-propelled dropwise condensate on superhydrophobic surfaces. *Phys. Rev. Lett.* **103** (18), 184501.

Brackbill, J.U., Kothe, D.B. & Zemach, C. 1992 A continuum method for modeling surface tension. *J. Comput. Phys.* **100** (2), 335–354.

Chandra, S. & Avedisian, C.T. 1991 On the collision of a droplet with a solid surface. *Proc. R. Soc.* A **432** (1884), 13–41.

Chantelot, P. 2018 Rebonds spéciaux de liquides. PhD thesis, Université Paris-Saclay (ComUE).

Cheng, X., Sun, T.-P. & Gordillo, L. 2021 Drop impact dynamics: impact force and stress distributions. *Annu. Rev. Fluid Mech.* **54**, 57–81.

Clanet, C., Béguin, C., Richard, D. & Quéré, D. 2004 Maximal deformation of an impacting drop. *J. Fluid Mech.* **517**, 199–208.

Culick, F.E.C. 1960 Comments on a ruptured soap film. *J. Appl. Phys.* **31**, 1128–1129.

Deka, H. & Pierson, J.-L. 2020 Revisiting the Taylor-Culick approximation. II. Retraction of a viscous sheet. *Phys. Rev. Fluids* **5**, 093603.

Dubrulle, B. 2019 Beyond Kolmogorov cascades. *J. Fluid Mech.* **867**, P1.

Eggers, J. 2018 Role of singularities in hydrodynamics. *Phys. Rev. Fluids* **3** (11), 110503.

Eggers, J., Fontelos, M.A., Josserand, C. & Zaleski, S. 2010 Drop dynamics after impact on a solid wall: theory and simulations. *Phys. Fluids* **22** (6), 062101.

Eyink, G.L. 1994 Energy dissipation without viscosity in ideal hydrodynamics I. Fourier analysis and local energy transfer. *Phys.* D **78** (3–4), 222–240.

Farokhirad, S., Morris, J.F. & Lee, T. 2015 Coalescence-induced jumping of droplet: inertia and viscosity effects. *Phys. Fluids* **27** (10), 102102.

Gordillo, J.M., Riboux, G. & Quintero, E.S. 2019 A theory on the spreading of impacting droplets. *J. Fluid Mech.* **866**, 298–315.

Gordillo, L., Sun, T.-P. & Cheng, X. 2018 Dynamics of drop impact on solid surfaces: evolution of impact force and self-similar spreading. *J. Fluid Mech.* **840**, 190–214.

Gorin, B., Di Mauro, G., Bonn, D. & Kellay, H. 2022 Universal aspects of droplet spreading dynamics in newtonian and non-newtonian fluids. *Langmuir* **38** (8), 2608–2613.

He, L., Ding, L., Li, B., Mu, W., Li, P. & Liu, F. 2021 Optimization strategy to inhibit droplets rebound on pathogen-modified hydrophobic surfaces. *ACS Appl. Mater. Interfaces* **13** (32), 38018–38028.

Jha, A., Chantelot, P., Clanet, C. & Quéré, D. 2020 Viscous bouncing. *Soft Matt.* **16** (31), 7270–7273.

Josserand, C. & Thoroddsen, S.T. 2016 Drop impact on a solid surface. *Annu. Rev. Fluid Mech.* **48**, 365–391.

Jowkar, S. & Morad, M.R. 2019 Rebounding suppression of droplet impact on hot surfaces: effect of surface temperature and concaveness. *Soft Matt.* **15** (5), 1017–1026.

Kim, J. 2007 Spray cooling heat transfer: the state of the art. *Intl J. Heat Fluid Flow* **28** (4), 753–767.

Kim, S., Wu, Z., Esmaili, E., Dombroskie, J.J. & Jung, S. 2020 How a raindrop gets shattered on biological surfaces. *Proc. Natl Acad. Sci. USA* **117** (25), 13901–13907.

Kolinski, J.M., Mahadevan, L. & Rubinstein, S.M. 2014 Drops can bounce from perfectly hydrophilic surfaces. *Europhys. Lett.* **108** (2), 24001.

Kolmogorov, A.N. 1941 The local structure of turbulence in incompressible viscous fluid for very large Reynolds numbers. *Dokl. Akad. Nauk USSR* **30**, 301–305.

LAAN, N., DE BRUIN, K.G., BARTOLO, D., JOSSERAND, C. & BONN, D. 2014 Maximum diameter of impacting liquid droplets. *Phys. Rev. Appl.* **2** (4), 044018.

LANDAU, L.D. & LIFSHITZ, E.M. 1987 *Fluid Mechanics – Volume 6: Course of Theoretical Physics*, 2nd edn. Elsevier.

LECOINTRE, P., MOUTERDE, T., CHECCO, A., BLACK, C.T., RAHMAN, A., CLANET, C. & QUÉRÉ, D. 2019 Ballistics of self-jumping microdroplets. *Phys. Rev. Fluids* **4** (1), 013601.

LIU, Y., CHEN, X. & XIN, J.H. 2008 Hydrophobic duck feathers and their simulation on textile substrates for water repellent treatment. *Bioinspir. Biomim.* **3** (4), 046007.

LIU, F., GHIGLIOTTI, G., FENG, J.J. & CHEN, C.-H. 2014 Numerical simulations of self-propelled jumping upon drop coalescence on non-wetting surfaces. *J. Fluid Mech.* **752**, 39–65.

LOHSE, D. 2022 Fundamental fluid dynamics challenges in inkjet printing. *Annu. Rev. Fluid Mech.* **54**, 349–382.

MOLÁČEK, J. & BUSH, J.W. 2012 A quasi-static model of drop impact. *Phys. Fluids* **24** (12), 127103.

MOUTERDE, T., LEHOUCQ, G., XAVIER, S., CHECCO, A., BLACK, C.T., RAHMAN, A., MIDAVAINE, T., CLANET, C. & QUÉRÉ, D. 2017*a* Antifogging abilities of model nanotextures. *Nat. Mater.* **16** (6), 658–663.

MOUTERDE, T., NGUYEN, T.-V., TAKAHASHI, H., CLANET, C., SHIMOYAMA, I. & QUÉRÉ, D. 2017*b* How merging droplets jump off a superhydrophobic surface: measurements and model. *Phys. Rev. Fluids* **2** (11), 112001.

NAIR, H., STAAT, H.J.J., TRAN, T., VAN HOUSELT, A., PROSPERETTI, A., LOHSE, D. & SUN, C. 2014 The leidenfrost temperature increase for impacting droplets on carbon-nanofiber surfaces. *Soft Matt.* **10** (13), 2102–2109.

NEINHUIS, C. & BARTHLOTT, W. 1997 Characterization and distribution of water-repellent, self-cleaning plant surfaces. *Ann. Bot.* **79** (6), 667–677.

ONSAGER, L. 1949 Statistical hydrodynamics. *Il Nuovo Cimento* **6** (2), 279–287.

PHILIPPI, J., LAGRÉE, P.-Y. & ANTKOWIAK, A. 2016 Drop impact on a solid surface: short-time self-similarity. *J. Fluid Mech.* **795**, 96–135.

PIERSON, J.-L., MAGNAUDET, J., SOARES, E.J. & POPINET, S. 2020 Revisiting the Taylor-Culick approximation: retraction of an axisymmetric filament. *Phys. Rev. Fluids* **5** (7), 073602.

PLANCHETTE, C., BIANCE, A.L. & LORENCEAU, E. 2012 Transition of liquid marble impacts onto solid surfaces. *Europhys. Lett.* **97** (1), 14003.

POPINET, S. 2009 An accurate adaptive solver for surface-tension-driven interfacial flows. *J. Comput. Phys.* **228** (16), 5838–5866.

POPINET, S. 2015 A quadtree-adaptive multigrid solver for the Serre-Green-Naghdi equations. *J. Comput. Phys.* **302**, 336–358.

POPINET, S. 2018 Numerical models of surface tension. *Annu. Rev. Fluid Mech.* **50**, 49–75.

POPINET, S. *et al.* 2013–2022*a* Basilisk C. Available at: http://basilisk.fr.

POPINET, S. *et al.* 2013–2022*b* Basilisk C: reduced pressure library. Available at: http://basilisk.fr/src/reduced.h.

PRANDTL, L. 1904 Über Flüssigkeitsbewegung bei sehr kleiner Reibung. Verhandl III, *Intern. Math. Kongr. Heidelberg, Auch: Gesammelte Abhandlungen* **2**, 484–491.

PROSPERETTI, A. & TRYGGVASON, G. 2009 *Computational Methods for Multiphase Flow*. Cambridge University Press.

QUÉRÉ, D. 2008 Wetting and roughness. *Annu. Rev. Mater. Res.* **38**, 71–99.

RAMÍREZ-SOTO, O., SANJAY, V., LOHSE, D., PHAM, J.T. & VOLLMER, D. 2020 Lifting a sessile oil drop from a superamphiphobic surface with an impacting one. *Sci. Adv.* **6** (34), eaba4330.

REIN, M. 1993 Phenomena of liquid drop impact on solid and liquid surfaces. *Fluid Dyn. Res.* **12** (2), 61.

RENARDY, Y., POPINET, S., DUCHEMIN, L., RENARDY, M., ZALESKI, S., JOSSERAND, C., DRUMRIGHT-CLARKE, M.A., RICHARD, D., CLANET, C. & QUÉRÉ, D. 2003 Pyramidal and toroidal water drops after impact on a solid surface. *J. Fluid Mech.* **484**, 69–83.

RICHARD, D., CLANET, C. & QUÉRÉ, D. 2002 Contact time of a bouncing drop. *Nature* **417** (6891), 811–811.

RICHARD, D. & QUÉRÉ, D. 2000 Bouncing water drops. *Europhys. Lett.* **50** (6), 769.

SANJAY, V. 2022*a* Code repository: when does a drop stop bouncing? Available at: https://github.com/VatsalSy/When-does-a-drop-stop-bouncing.

SANJAY, V. 2022*b* Viscous free-surface flows. PhD thesis, University of Twente, Netherlands.

SANJAY, V., LAKSHMAN, S., CHANTELOT, P., SNOEIJER, J.H. & LOHSE, D. 2023 Drop impact on viscous liquid films. *J. Fluid Mech.* **958**, A25.

SANJAY, V., SEN, U., KANT, P. & LOHSE, D. 2022 Taylor–Culick retractions and the influence of the surroundings. *J. Fluid Mech.* **948**, A14.

SARMA, B., DALAL, A. & BASU, D.N. 2022 Interfacial dynamics of viscous droplets impacting a superhydrophobic candle soot surface: overview and comparison. *Phys. Fluids* **34** (1), 012121.

SHIRI, S. & BIRD, J.C. 2017 Heat exchange between a bouncing drop and a superhydrophobic substrate. *Proc. Natl Acad. Sci. USA* **114** (27), 6930–6935.

TAI, Y., ZHAO, Y., GUO, X., LI, L., WANG, S. & XIA, Z. 2021 Research on the contact time of a bouncing microdroplet with lattice Boltzmann method. *Phys. Fluids* **33** (4), 042011.

TAYLOR, G.I. 1959 The dynamics of thin sheets of fluid. III. Disintegration of fluid sheets. *Proc. R. Soc. London, Ser. A* **253**, 313–321.

THORODDSEN, S.T., ETOH, T.G. & TAKEHARA, K. 2008 High-speed imaging of drops and bubbles. *Annu. Rev. Fluid Mech.* **40**, 257–285.

TRYGGVASON, G., SCARDOVELLI, R. & ZALESKI, S. 2011 *Direct Numerical Simulations of Gas–Liquid Multiphase Flows*. Cambridge University Press.

TSAI, P., PACHECO, S., PIRAT, C., LEFFERTS, L. & LOHSE, D. 2009 Drop impact upon micro-and nanostructured superhydrophobic surfaces. *Langmuir* **25** (20), 12293–12298.

VILLERMAUX, E. & BOSSA, B. 2011 Drop fragmentation on impact. *J. Fluid Mech.* **668**, 412–435.

DA VINCI, L. 1508 *Codex Leicester* (ed. and transl. E. MacCurdy), The Notebooks of Leonardo da Vinci. George Braziller.

WACHTERS, L.H.J. & WESTERLING, N.A.J. 1966 The heat transfer from a hot wall to impinging water drops in the spheroidal state. *Chem. Engng Sci.* **21** (11), 1047–1056.

WILDEMAN, S., VISSER, C.W., SUN, C. & LOHSE, D. 2016 On the spreading of impacting drops. *J. Fluid Mech.* **805**, 636–655.

WORTHINGTON, A.M. 1877*a* On the forms assumed by drops of liquids falling vertically on a horizontal plate. *Proc. R. Soc. Lond. Ser.* A **25** (171–178), 261–272.

WORTHINGTON, A.M. 1877*b* A second paper on the forms assumed by drops of liquids falling vertically on a horizontal plate. *Proc. R. Soc. Lond.* **25**, 498–503.

XU, L., ZHANG, W.W. & NAGEL, S.R. 2005 Drop splashing on a dry smooth surface. *Phys. Rev. Lett.* **94** (18), 184505.

YARIN, A.L. 2006 Drop impact dynamics: splashing, spreading, receding, bouncing…. *Annu. Rev. Fluid Mech.* **38**, 159–192.

ZHANG, B., SANJAY, V., SHI, S., ZHAO, Y., LV, C. & LOHSE, D. 2022 Impact forces of water drops falling on superhydrophobic surfaces. *Phys. Rev. Lett.* **129**, 104501.